Next Materials 8 (2025) 100573

Contents lists available at ScienceDirect

Next Materials

journal homepage: www.sciencedirect.com/journal/next-materials

Research article

Synthesis, and explication of structural and optical characteristics of $Ba_3Co_2O_6(CO_3)_{0.6}$

Fareenpoornima Rafiq [a,1,*], Sumathi Jones [b,2], Papitha Purushothaman [c,3]

[a] Department of Physics, Vel Tech Multi Tech Dr Rangarajan Dr Sakunthala Engineering College, Chennai 600 062, India
[b] Department of Pharmacology, Sree Balaji Dental College and Hospital, Bharath University, Chennai 600100, India
[c] Department of Computer Science, Dr MGR Educational and Research Institute, Chennai 600095, India

ARTICLE INFO

Keywords:
Dislocation density
Refractive index
Herve–Vandamme formula
Photoluminescence

ABSTRACT

The nanostructured powder sample, $Ba_3Co_2O_6(CO_3)_{0.6}$ was fabricated by sol-gel method. The powder XRD pattern revealed a 37 nm-sized crystallite, P-6 symmetric hexagonal structure, anisotropic with a plate-like morphology. By examining the absorption spectrum, the optical parameters have been computed in the wavelength range of 400–1000 nm. Tauc's direct transition model is used to characterize the optical absorption edge, and its extrapolation yields the optical band gap (E_g) to be 3.12 eV. The refractive index using Herve–Vandamme formula for the synthesized sample was 2.39. PL spectra of $Ba_3Co_2O_6(CO_3)_{0.6}$ was measured at room temperature by a Fluoromax3 Spectroflourimeter – Perkin Elmer LS 45. shows the properties of direct band gap material. PL study which encompasses the whole visible area of the electromagnetic spectrum, revealed the weak emission band at 440 nm symbolizing blue-green emission, generating a red-shifted narrow emission band at 766 nm. Energy gap values and PL emission suggest the synthesized sample's semiconducting nature. The optical properties of synthesized nanostructured samples find their importance in solar cells, electrochromic devices, and gas sensor applications.

1. Introduction

The unique characteristics of nanocrystals, which rely on the particle size at the nanoscale, include phase transition temperature, melting point, and improved solubility [1]. The primary sources of the special characteristics of nanocrystalline materials, which set them apart from bulk ones, are quantum confinement effects and the increased function of surface atoms with decreasing particle size. Transition metal oxide (TMO) nanoparticles, in particular, have drawn much attention with their physical characteristics. TMOs have been the subject of much research due to their spin-polarization, magnetic, optical, solar cell, and antibacterial characteristics. The experimental conditions have a significant impact on the properties of metal oxide nanomaterials, such as particle size, shape, and stability [2]. Due to its optical transparency, mechanical stability, chemical resistance, and adaptability in sensor morphological designs, sol-gel-derived materials have drawn special attention as chemical receptor matrices. The materials have many benefits, including the ability to be set up at room temperature, the fact that they are not broken down by light or electrochemical processes, they can undergo a wide range of chemical changes, can be obtained in different forms (such as monoliths, thin films, fibers, or powders), and they react quickly. These materials are desirable for application in the food, chemical, and pharmaceutical sectors because of the combination of these qualities [3]. Cobalt oxide, which may be made in a variety of ways, is seen as a promising material since it can be used as a highly selective CO sensor, a photocatalyst, a solar selective absorber at high temperatures, a thin-film supercapacitor electrode material in electrochromic devices, and a magnetic material, as a result of altering its optical characteristics in response to an external electrical stimulus [4,5]. The precise optical characteristics of Co_3O_4 nanoparticles can change based on the dopants, crystal structure, and production techniques employed [1]. From the literature [6,7], it has been found from the density functional theory (DFT) of the electronic behavior of alkaline earth metals Ca and Ba dopants in $Na_{0.75}CoO_2$, that both Ca and Ba

* Corresponding author.
E-mail address: fahreenpoornima@gmail.com (F. Rafiq).
[1] https://orcid.org/0000-0002-9237-9673
[2] https://orcid.org/0000-0003-3192-6247
[3] https://orcid.org/0009-0002-3421-9003

https://doi.org/10.1016/j.nxmate.2025.100573
Received 1 November 2024; Received in revised form 26 February 2025; Accepted 27 February 2025
Available online 17 March 2025
2949-8228/© 2025 The Author(s). Published by Elsevier Ltd. This is an open access article under the CC BY-NC-ND license (http://creativecommons.org/licenses/by-nc-nd/4.0/).

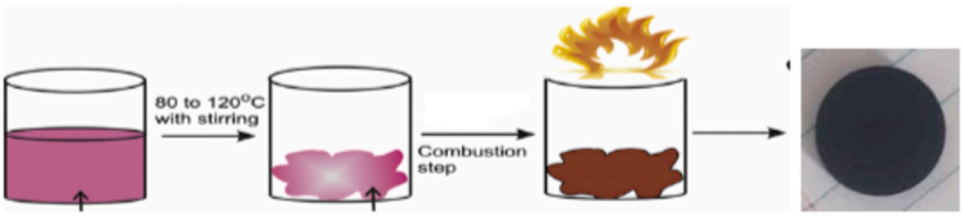

Fig. 1. Schematic representation of sol-gel combustion synthesis.

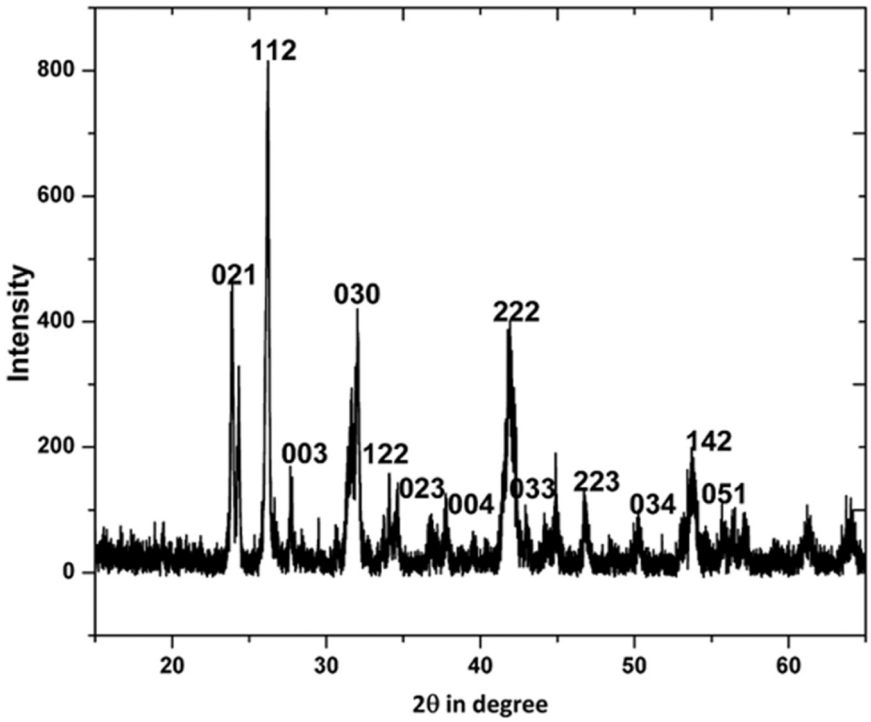

Fig. 2. XRD patterns with hkl values of $Ba_3Co_2O_6(CO_3)$.

dopants tend to substitute Na sites instead of Co sites and the margin of stability in the case of Ba is greater than the one of Ca. The study also shows that the substitution of La^{2+} by divalent ions in $LaCoO_3$, such as Ca^{2+}, Sr^{2+} and Ba^{2+} has a significant influence on the spin state of Co^{3+}/Co^{4+}, oxygen vacancy concentration and/or crystal-structure distortions in the material, which also affect the physical (electric and magnetic) properties [8]. It has also been reported that an interesting insulator-metal (I-M) transition occurs when either temperature or A's ionic radius increases in a misfit-layered $Bi_2A_2Co_2O_6$, concluding that misfit-layered $Bi_2A_2Co_2O_6$ is likely to take a metallic state at a larger lattice constant while staying in an insulator state at a smaller lattice constant [9]. Additionally, the addition of a foreign element to the host may take the place of an atom from the metal framework by occupying an interstitial site even at low temperatures and can alter the host's physicochemical characteristics, such as phase transitions, changes in the lattice parameter, thermal stability, etc [10]. The necessity for novel synthesis techniques in the nuclear firm led to the development of the sol-gel method in the 1960s. A technique that required a lower sintering temperature and produced less dust than the ceramic process was needed. Furthermore, the synthesis ought to be able to be controlled remotely. Materials with a range of morphologies, including porous structures, thin fibers, dense powders, and thin films, can be created using sol-gel synthesis. The main use of a wet-chemical process is the creation of materials, usually metal oxides, from a chemical solution (sol, short for solution), which serves as the starting point for an integrated network (or gel) of network polymers or discrete particles. Because of the features like the capacity to produce inorganic nanoparticles with excellent purity, excellent nanostructure homogeneity, broad suitability for a range of inorganic materials, regulation of the structures' particle size and shape, the ability to create phases that are nanoporous, regulation of the particles' crystallinity, a process with a comparatively low temperature, etc., the approach has garnered a lot of study interest recently. By intimately mixing the reactant cations on an atomic scale, the sol-gel method's constituent hydroxyl groups may be involved in intra- or intermolecular interactions. This increases the reaction rate, which lowers the synthesis temperature and produces smaller particles.

Photoluminescence spectra are often employed to reveal the performance of electron-hole pairs in semiconductors i.e., to access the recombination rate of photogenerated (e^-/h^+) pairs in the synthesized sample. There are two phases in the fundamental mechanism of PL emission. The first involves the substance being electronically excited by incident radiation, while the second involves the excited photon's subsequent emission. The emission process is separated into fluorescence and phosphorescence based on the time that passes between these processes. Phosphorescence can have a comparatively longer delay time and the decay time of $\sim 10^{-8}$ s might be thought of as the point at which fluorescence and phosphorescence diverge. Furthermore, if the energy emitted or absorbed equals the difference between the stimulated and ground levels, the emission process is considered radiative. Conversely,

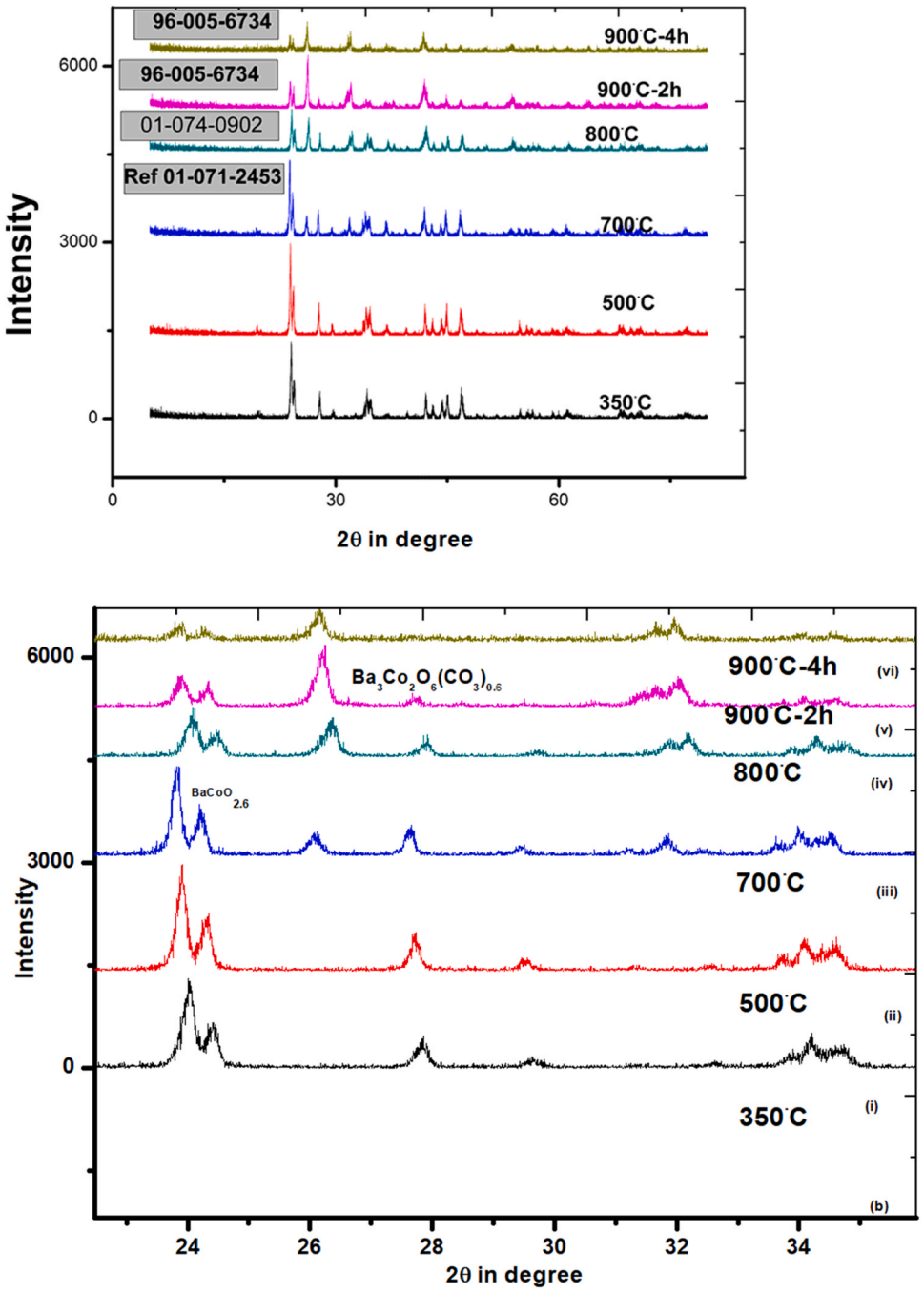

Fig. 3. (a). XRD patterns of the synthesized sample at different temperatures and (b) High intensity peaks- projected.

a nonradiative process illuminates a tiny portion of the absorbed energy, with the remaining energy being lost via heat radiation, phonon excitations in solids, or molecular vibrations [11]. Specifically, the features of photoluminescence (PL) are a significant quantum optical phenomenon and one of the most effective ways to investigate order-disorder effects in semiconductors. The optical properties of semiconductor materials are significantly impacted by structural and electrical order-disorder phenomena. When the degree of local order is high enough that structurally inequitable sites can be identified by their various electronic transition types and are associated with a particular structural arrangement, PL is an intriguing method for probing specific structural aspects to provide information at the short- and medium-range. There is ongoing interest in the synthesis of noble nanoparticles for use in biology, electronics, environmental, and catalytic applications [12]. In most cases, the degree of structural and electrical disorder in the lattice controls the optical band gap energies, allowing for a change in the optical transitions and providing a chance to adjust their characteristics through the band gap [13].

We report the synthesis of $Ba_3Co_2O_6(CO_3)_{0.6}$ nanoparticles utilizing nitrates in the sol-gel method with a shorter annealing time, even though the synthesis and thermoelectric properties have been documented previously. As far as we are aware, this is the first report on the optical characteristics of the synthesized sample, $Ba_3Co_2O_6(CO_3)_{0.6}$ nanoparticles including absorbance, refractive index, and photoluminescence.

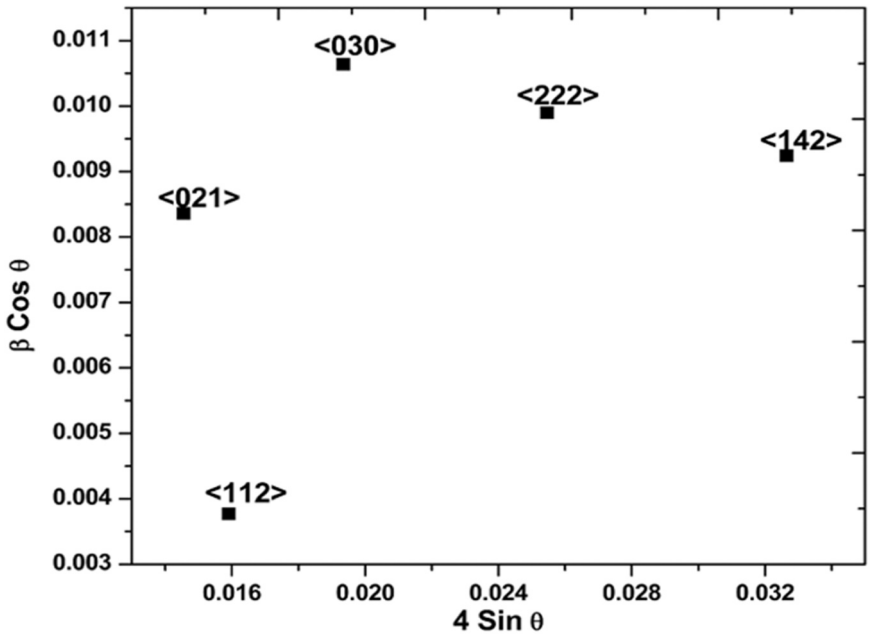

Fig. 4. W-H analysis of $Ba_3Co_2O_6(CO_3)_{0.6}$.

Table 1
Observed and calculated diffraction angles, D-spacing, and crystallite size with (hkl) planes $Ba_3Co_2O_6(CO_3$ nanoparticles.

Observed diffracting angle, 2θ (degree)	Calculated diffracting angle, 2θ (degree)	Observed D-spacing (Å)	Calculated D-spacing (Å)	hkl planes	Crystallite size D (nm)	Lattice parameter of the sample (Å)
26.25	26.15	2.70	3.40	112	65.79	4.14
23.97	23.39	3.63	3.80	021	29.56	8.74
32.01	32.05	2.80	2.79	030	23.60	3.16
41.98	41.86	2.12	2.16	222	26.18	8.01
53.71	53.67	1.70	1.71	142	34.54	7.03
37.76	37.78	2.38	2.38	004	81.50	3.77

2. Experimental section

2.1. Materials and methods

Barium nitrate ($BaNO_3$,99.9 % purity) and cobalt nitrate hexahydrate ($Co(NO_3)_2.6H_2O$; 99.9 % purity) were acquired from Sigma Aldrich and were put to use without any additional purification. Ethanol and citric acid were utilized as the solvent. The stoichiometric amounts of the precursor powders, barium nitrate, the cobalt (II) nitrate were added to the solvent ethylene glycol and the complexing agent, citric acid, and were stirred vigorously using a magnetic stirring bar for 3 h at the 120 ℃ same temperature. High effervescence and a shift in color from red to purple were seen during this procedure. The deep purple frothy material was manually crushed to break up the agglomerates and kept in a furnace wherein the auto-combustion took place (300 ℃). The resultant ash product was calcined at 900 ℃ for 2 h in a furnace with an atmosphere of air, and a homogeneous powder sample with nanoscale particle size was produced. [14]. The quick synthesis of the beginning precursors at relatively low temperatures is a benefit of the auto-combustion reaction and makes it possible to keep the subsequent calcination time necessary to create the $Ba_3Co_2O_6(CO_3)_{0.6}$ phase reasonably short, 2 h in the present study [15,16]. Fig. 1 depicts the procedure of the synthesis. Earlier we have reported on the phase change of the annealing temperature and the mixed conduction of the sample [17,18]. Investigations have been made into the associated properties of the end product of the present synthesis.

2.2. Instrumentation

The heat-treated nano-powder sample's shape and microstructures were analyzed using electron microscopy FESEM (Carl Zeiss, ZIGMA / BRUKER) with an energy dispersive spectroscopy; X-ray diffraction using Bruker-axs D8 diffractometer (40KV, 30 mA) controlled by DIFFRAC plus software, in Bragg- Brentano reflection geometry with Cu Kα radiation (=1.05418 Å); Far-Infrared spectra (FT-IR) from the sample was observed in the 400–4000 cm^{-1}via Fourier transform-infrared spectrometer (Perkin-Elmer spectrum); UV-Vis spectroscopy study using UV+ t90 spectrometer and photoluminescence via Spectroflourimeter – Perkin Elmer LS 45.

Origin 8.6 software was used in the graphical analysis.

3. Results and discussion

3.1. Structural characterization

Fig. 2 displays the XRD pattern of the produced $Ba_3Co_2O_6(CO_3)_{0.6}$ sample. The different crystalline phases present in the sample were confirmed by comparing the XRD pattern to reference phases of the Xpert high score plus software. Major peaks had been associated with the $Ba_3Co_2O_6(CO_3)_{0.6}$ phase, specified by its reflection planes (Fig. 2). The acquired data indicate that the crystal planes (112), (021), (030), (222), (142), and (004) all have intensity peaks, with the highest intensity peak being found at (112), picturized in Fig. 2. The JCPDS file (PDF no: 01–070–3621) and the previously published report [17,19] are in good agreement with all of the peaks that have been identified. A rich

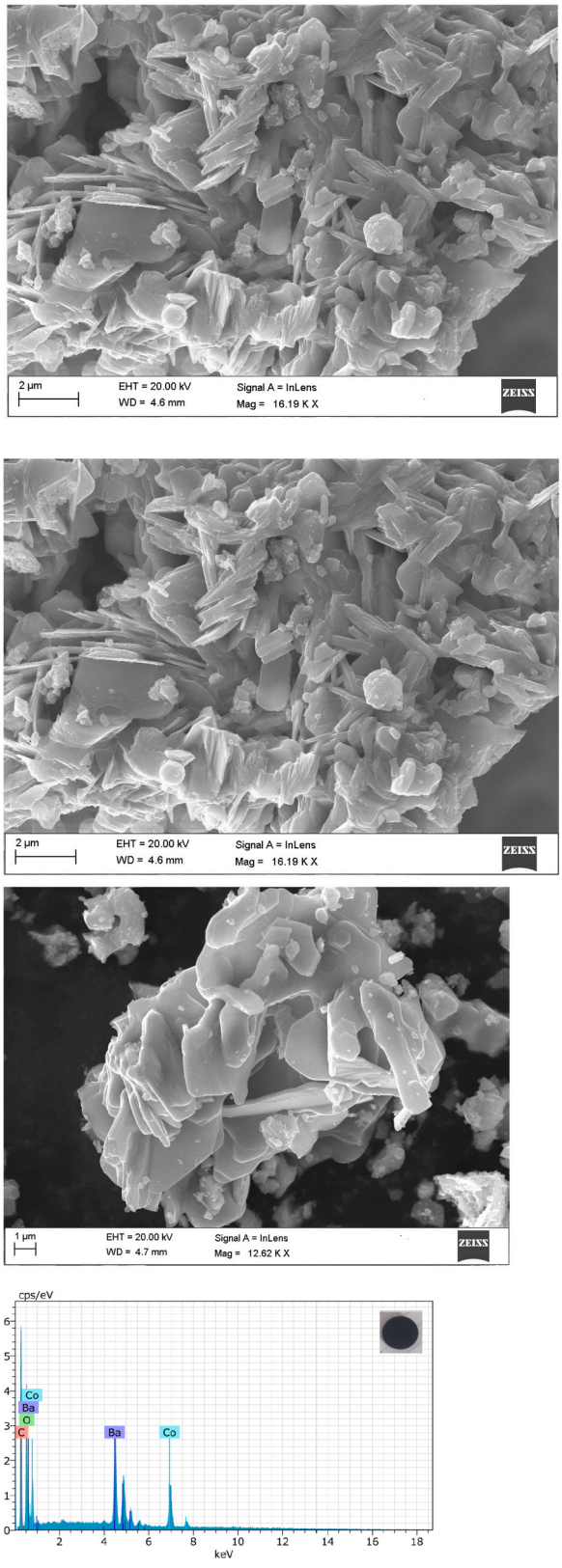

Fig. 5. FESEM photographs with different magnifications & EDX spectrum of $Ba_3Co_2O_6(CO_3)_{0.6;}$ Inset: Synthesized pellet sample.

oxygen atmosphere during sintering could have stabilized the $Ba_3Co_2O_6(CO_3)_{0.6}$ phase, suppressing the formation of stoichiometric $Ba_3Co_4O_9$ [20]. The production polycrystalline $Ba_3Co_2O_6(CO_3)_{0.6}$ (space group: P-6) with a hexagonal structure is seen [19]. As pointed out in the literature, the structure can be explained by a hexagonal stacking sequence of Ba_3O_{9-y} layers (y = 1.2), with P-6 symmetry in which two-thirds of the octahedral sites defined by the oxygen atoms are occupied in an orderly manner by Co atoms. Rows of face-sharing octahedra running along the c-axis are created by the orderly occupation of octahedral sites; two of these rows are occupied by cobalt, while the third Co-free row contains the carbonate groups at random. $Ba_3Co_2O_6(CO_3)_{0.60}$ structure can be described from the ordered intergrowth of two blocks, $[Ba_2Co_2O_6]_{\delta-}$ and $[Ba(CO_3)_{0.60}]_{\delta+}$, alternating along the a-axis and hence, formulated as $Ba_3Co_2O_6(CO_3)_x$. [19,21] IR spectroscopy suggests the presence of carbonate groups in the structure. Fig. 3 depicts the various phases associated with the synthesized sample constituting different temperatures. A series of phase changes ($BaCoO_{2.6}$→$BaCoO_3$→$Ba_3Co_2O_6(CO_3)_{0.6}$) from 973 K to 1173 K complicate the phase sequence. Therefore, 900℃ for two h may be considered the start-up temperature for the synthesis of $Ba_3Co_2O_6(CO_3)_{0.6}$. In our earlier work, we have discussed the properties of $BaCoO_{2.6}$ and Mg- substituted $BaCoO_{2.6}$ [17,18].

The Scherrer equation (Eq. 1),

$$D = \frac{k\lambda}{\beta Cos\theta} \tag{1}$$

with k = 0.9, and, the full width at half maximum (FWHM) of the main plane (112) were utilized to estimate the size of the crystallite [22].

The dislocation density from Eq. 2,

$$\delta = \frac{1}{D^2} \tag{2}$$

was discovered to be 7.39×10^{14} lines/m^2 and the calculated crystallite size was in the nanometer range (36.78 nm). The secondary phases were greatly reduced upon annealing at 1173 K. The scattered spots in the Williamson-Hall (Fig. 4) graph indicate that the synthesized sample is anisotropic in nature [20].

The spacing between diffracting planes (d) of synthesized $Ba_3Co_2O_6(CO_3)$ nanoparticles was calculated from the Bragg equation (equation 3),

$$n\,\lambda = 2d\,Sin\,\theta \tag{3}$$

The lattice parameter of the cubic (a = b = c) and hexagonal (a = b ≠ c) crystal is calculated using the formula (Eq. 4),

$$\frac{1}{d^2} = \frac{h^2}{a^2} + \frac{k^2}{a^2} + \frac{l^2}{a^2} \text{and} \frac{1}{d^2} = \frac{h^2}{a^2} + \frac{k^2}{a^2} + \frac{l^2}{c^2} \tag{4}$$

where, d is the atomic lattice spacing, h, k and l are Miller indices; a is the lattice parameter of the crystal [22,23]. The microstructure data of $Ba_3Co_2O_6(CO_3$ has been tabulated (Table 1).

Fig. 5 displays the FESEM images having agglomerates of very thin, non-uniform plate-like morphology with mean grain sizes that have been estimated to be in the range of ~1–5 µm, in the planar dimension and are consistent with the other data found in the literature [24–27] and the EDS spectrum verifies the presence of Ba, Co, C and O elements in the synthesized sample.

$Ba_3Co_2O_6(CO_3)_{0.6}$'s FTIR pattern is depicted in Fig. 6. The presence of carbonate groups, which may be caused by the substitution of some Co_3^{2-} by CO_3^{2-} ions, is what is responsible for the occurrence of peaks in the regions of 1449 cm^{-1} and 856 cm^{-1} [28]. Co-O stretching vibrations are responsible for the absorption band at 664 cm^{-1}, and the doublets around 570 cm^{-1} show two valence states for the cobalt ions connected to Co-O vibrations [29]. Water absorption is responsible for the H-O-H mode peaks at 1636 cm^{-1}.

Fig. 7 depicts thermal experiments (TG/DSC) from ambient temperature to 600℃. A solid-state endothermic reaction can be observed to have taken place during heating given that the heat flow between the two peaks was non-linear. The endothermic peak on the DSC curve at

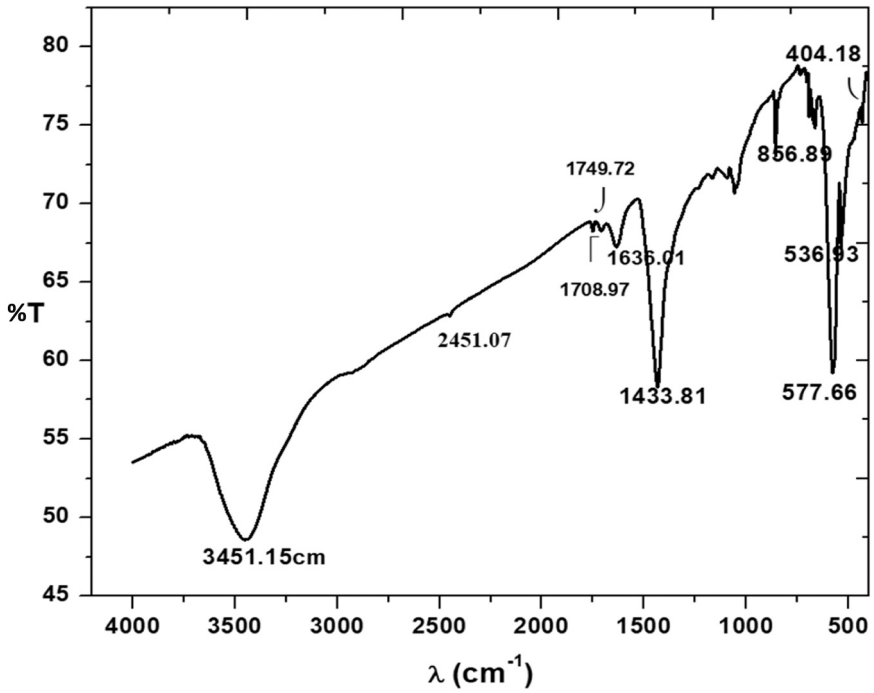

Fig. 6. FTIR spectrum.

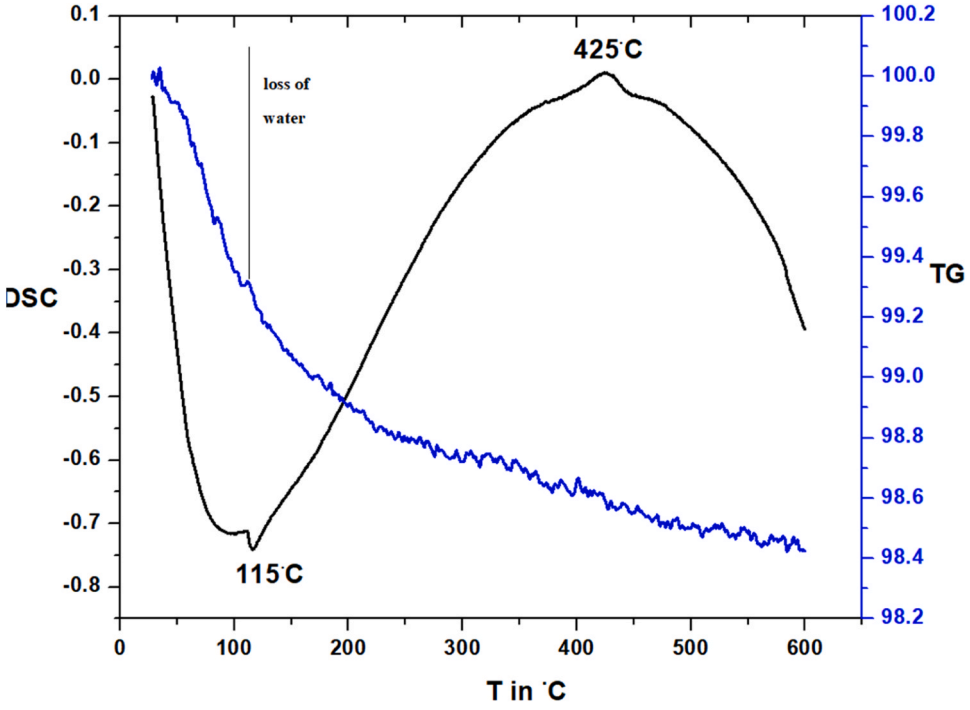

Fig. 7. DSC-TG curves of $Ba_3Co_2O_6(CO_3)_{0.6}$.

112 °C may represent the melting point of the sample [30] According to the tiny peak around 430 ℃, the symmetry change is an exothermic event, which may be due to the formation of gaseous products and affirms the formation of phase [15,31]. After 300 ℃, decomposition begins, and until the measured temperature of 600 ℃ (TG curve), only a little weight loss of about 1.6 mg is seen.

3.2. Optical study

Many molecules absorb visible or ultraviolet light when a particular frequency of light passes through them, and the transmittance light radiation % is calculated in UV-Vis spectrophotometric analysis. This method calculates the absorbance intensity or optical density (O.D.) as a function of wavelength. According to Beer's law, the concentration of the absorbing species directly correlates with absorption [26]. The absorbance curve in the Fig. 8 displays a pronounced peak around

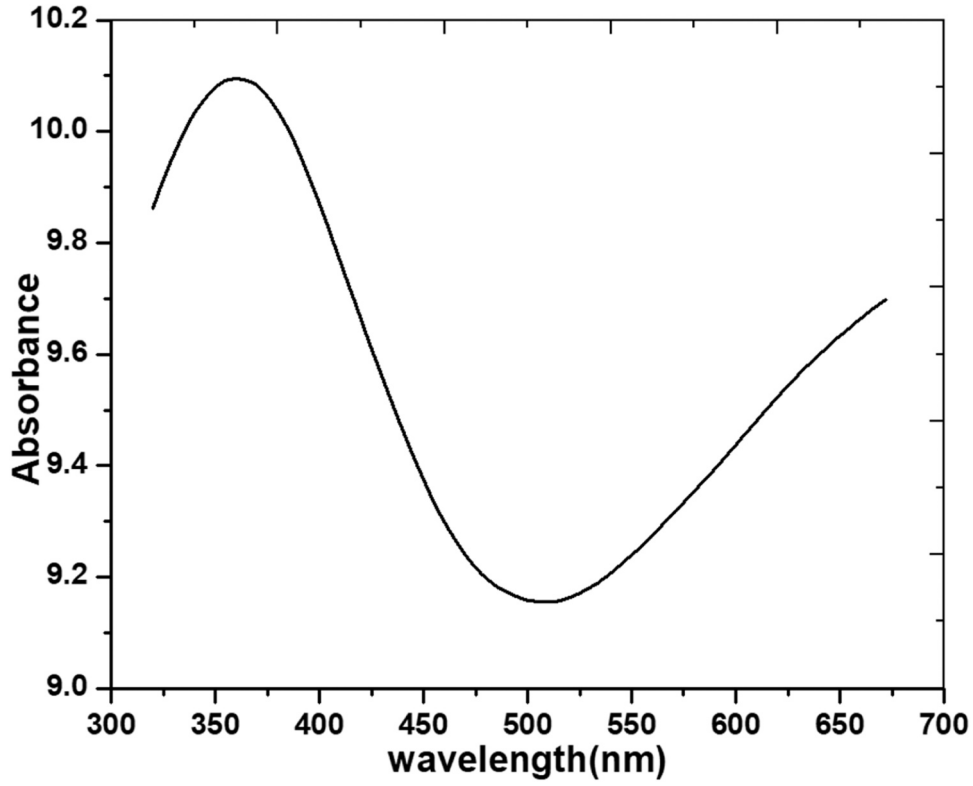

Fig. 8. Absorbance spectrum of $Ba_3Co_2O_6(CO_3)_{0.6}$.

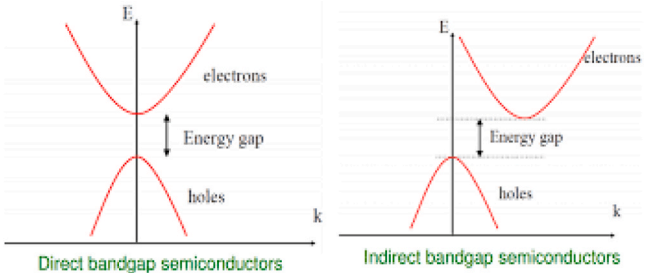

Fig. 9. The valence (VB) and conduction (CB) bands of direct and indirect bandgap semiconductors are depicted in this simplified energy diagram.

362 nm from the plasmon resonance of $Ba_3Co_2O_6(CO_3)_{0.6}$ nanoparticles. [27]. Highly crystalline nanoparticles with fewer surface flaws are demonstrated by the abrupt increase in the spectra at the absorption edge [1].

The absorption of radiation dealing with the electronic transition between the valence band and conduction band is categorized into direct and indirect band transitions (Fig. 9). The energy gap (E_g) can be determined from Tauc's plot (αhυ vs hυ) and the relation (Eq. 5),

$$\alpha h\upsilon = A(h\upsilon - E_g)^{\beta} \tag{5}$$

where A is a constant, υ is the transition frequency, and the exponent (β) characterizes the nature of band transitions, wherein β= 1/2 & 3/2 corresponds to direct allowed and directly forbidden transitions and β= 2 & 3 to indirect allowed & forbidden transitions, respectively. Extrapolating the straight line Tauc's graph to hυ = 0 of Fig. 10 with the best straight-line fit of β = 2 for the direct transition [14,16,19] quantifies the energy gap (E_g) of 3.12 eV, suggesting that the produced nanoparticles are primarily semiconductors [28]. The energy gap of the crystalline materials depends on their anisotropy, temperature, and pressure under an electromagnetic field and microstructural constituents like short-term coordination and nano- & micro crystallites, etc., [26,27].

Electronic polarization of ions and the local field inside the optical material are examples of intrinsic material properties that are related to the material's refractive index. It is evident that as photon energy increases, the produced material's refractive index drops, indicating that the synthesized polymeric samples exhibit typical dispersion behavior. The interaction between photons and electrons is demonstrated by the change in n values with photon energy. Since the internal energy of the device depends on the photon energy, we may estimate the photon energy to obtain the necessary material for building the optoelectronics device [29,32].

The variation of the refractive index 'n' has been evaluated by the expression (Eq. 6) [33].

$$n = \frac{1+\sqrt{R}}{1-\sqrt{R}} \tag{6}$$

where 'R' is the reflectance of the material. The maximum value of the refractive index was found to be 1.67 for the wavelength of 204 nm, depicted in Fig. 11.

The Herve–Vandamme formula was also used to determine the $Ba_3Co_2O_6(CO_3)_{0.6}$ powder sample's refractive index, (Eq. 7) [23],

$$n = \left[1 + \left(\frac{P}{E_g + Q}\right)^{2}\right]^{1/2} \tag{7}$$

where the typical constant values are P = 13.6 eV and Q = 3.4 eV. The refractive index determines the density measurement and provides information about the vacancies in the $Ba_3Co_2O_6(CO_3)_{0.6}$ nanoparticles and was found to be 2.39.

The produced $Ba_3Co_2O_6(CO_3)_{0.6}$ nanoparticles with 380 nm excitation exhibit the greatest PL emission in the 400–800 nm wavelength range, which encompasses the whole visible area of the electromagnetic spectrum. Fig. 12 displays the narrow PL peak at 766 nm and the weak broad peak at 440 nm. The emission band seen at 440 nm (about 3.5 eV)

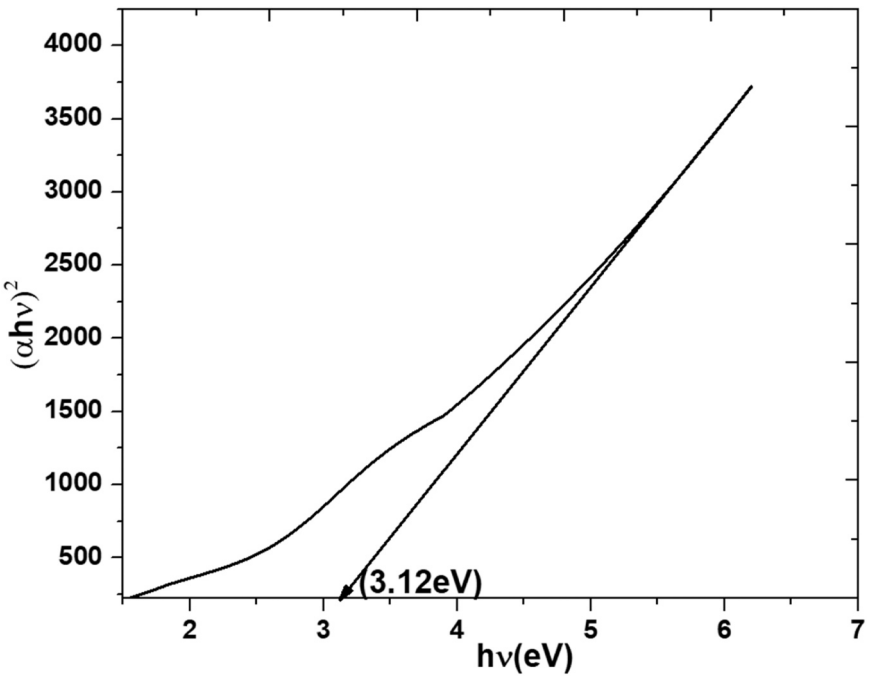

Fig. 10. Tauc plot (direct transition) of $Ba_3Co_2O_6(CO_3)_{0.6}$.

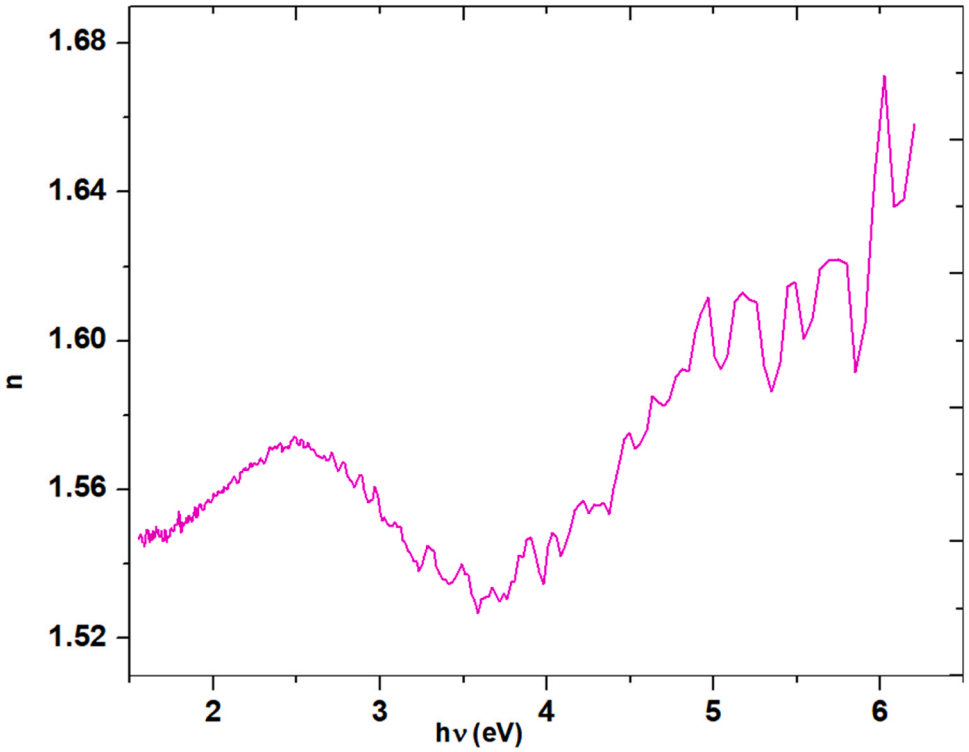

Fig. 11. Refractive index versus photon energy for $Ba_3Co_2O_6(CO_3)_{0.6}$.

may be caused by the relative oxygen vacancies (surface defects) of the nanoparticles, which shall be explained via the charge carrier transfer between the conduction and valence bands of the nanoparticles [34] by quantum confinement [35] or due to the band edge emission [22] because the peak value roughly corresponds to the $Ba_3Co_2O_6(CO_3)_{0.6}$ nanoparticles band gap, indicating the blue-green colored emission [36]. The radiative recombination mechanism, which was caused by exciton entrapment at the localized stationary states (LSS) and usually connected to the NPs sizes, was identified as the cause of the observed narrow emission band at 766 nm for the $Ba_3Co_2O_6(CO_3)_{0.6}$ NPs in the energy range 1.62 eV significantly lower than the band gap. The major resource of trap states in the suggested NPs was primarily the surface area to volume ratio. Additionally, LSS atoms have un-passivated valence bonds (dangling states) because they have fewer neighboring atoms than their bulk (interior). These unsaturated atomic orbitals may result in additional energy states (referred to as LSSs) in the synthesized

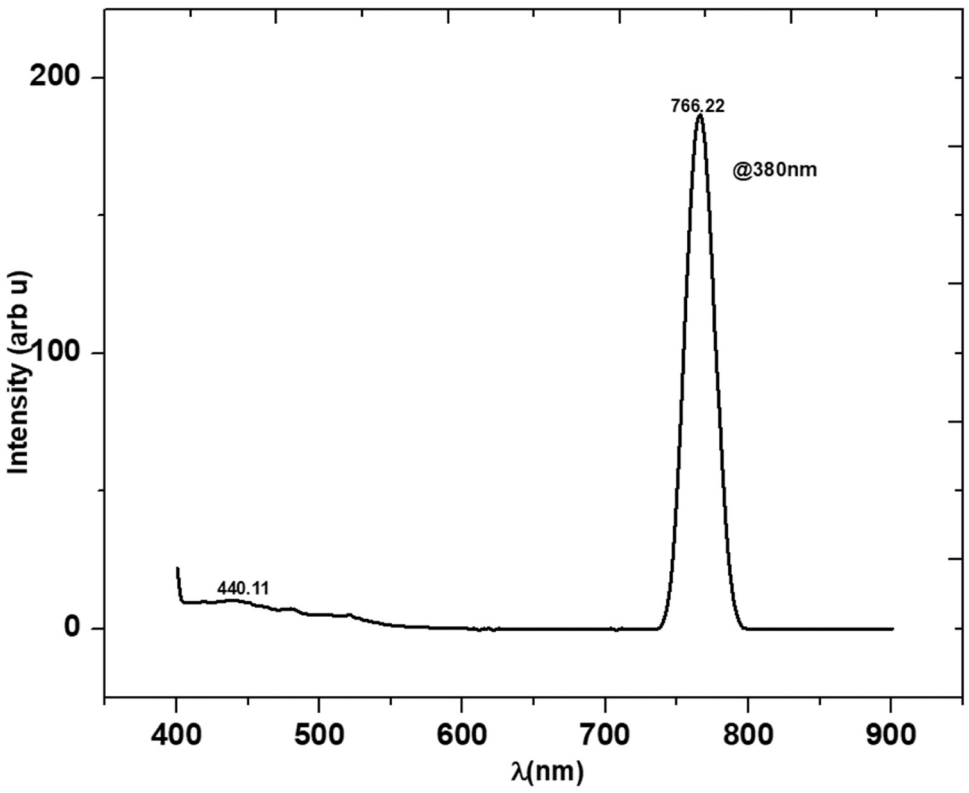

Fig. 12. Photoluminescence spectrum of $Ba_3Co_2O_6(CO_3)_{0.6}$.

NPs HOMO–LUMO band gap, which is in charge of exciton trapping and ultimately visible light emission by radiative recombination [11,36]. Oxygen vacancies in the particle's crystalline systems generate a noticeable redshift in the synthesized sample's PL behavior indicating a change in the local chemical environment and disorder and the expectation that specific localized states should exist in the forbidden band gap [37–39]. Meanwhile, the lower energy peak may come from the emission of defects such as O^{2-} vacancies [40,41]. Fast electron-hole recombination typically produces a greater PL signal, and vice versa. Thus, a reduction in PL intensity due to the decrease in electron-hole recombination rate builds up photocatalytic efficiency. [42,43]

4. Conclusion

In the current research, our synthesis using the sol-gel method yielded nano-sized particles of 37 nm with a hexagonal structure of P-6 symmetry. SEM analysis depicts plate-shaped grains, and EDAX confirmed the expected elements. The scattered plot of Williamson-Hall suggests the sample's anisotropic nature. UV-Vis optical study elucidated the absorption wavelength of 362 nm, and Tauc's direct transition yields the optical band gap (E_g) to be 3.12 eV. The refractive index using the Herve–Vandamme formula for the synthesized sample was found to be 2.39. PL study, which encompasses the whole visible area of the electromagnetic spectrum, revealed the weak emission band at 440 nm symbolizing blue-green emission, generating a red-shifted narrow emission band at 766 nm. Energy gap values and PL emission suggest the synthesized sample's semiconducting nature. The optical properties of synthesized nanostructured samples find their importance in solar cells, electrochromic devices, and gas sensor applications. More insight into its linear and non-linear optical properties and photocatalytic applications of $Ba_3Co_2O_6(CO_3)_{0.6}$ nanoparticles will be our future research.

Declaration of Competing Interest

The authors declare that they have no known competing financial interests or personal relationships that could have appeared to influence the work reported in this paper.

Acknowledgments

One of the authors (Fareenpoornima Rafiq) would like to thank the Department of Physics, Loyola College, Chennai for UV-Vis studies and the Department of Physics, St Joseph's College, Trichy for the photoluminescence study.

Authors contributions

Ms Fareenpoornima Rafiq (Author1) carried out the synthesis process, and analysis of various studies and drafted the manuscript. Dr. Sumathi Jones (Author2) helped procure materials for synthesis, discussion of results and sequence alignment. Ms Papitha P (Author 3) helped analyze the graphs. All authors read and approved the final manuscript.

Data availability

The data to support the findings of the study are included in the article

References

[1] Indira Priyadharsini, M. Sumathi, A. Prakasam, P.M. Anbarasan, R. Sathiyapriya, V. Aroulmoji, Effect of Mg doping on structural and optical properties of SnO_2 nanoparticles by chemical co-precipitation method, Int. J. Adv. Sci. Eng. 3 (4) (2017) 428–434.

[2] Soressa Desta Karse, Misganu Chewaka Fite, Studies on structural and optical properties of cobalt oxide nanoparticles using co-precipitation, Phys. B: Condens. Matter 689 (2024) 416181, https://doi.org/10.1016/j.physb.2024.416181.

[3] Jun Zhang, Su-Qing Zhao, Kun Zhang, Jian-Qing Zhou, Yan-Fei Cai, A study of photoluminescence properties and performance improvement of Cd-doped ZnO quantum dots prepared by the sol-gel method, Nano Express 7 (2012) 405.

[4] Salah A. Makhlouf, Zinab H. Bakr, Kamal I. Aly, M.S. Moustafa, Structural, electrical and optical properties of Co_3O_4 nanoparticles, Superlattices Microstruct. 64 (2013) 107–117, https://doi.org/10.1016/j.spmi.2013.09.023.

[5] Maragoni Venkatesham, Dasari Ayodhya, Alle Madhusudhan, Amrutham Santoshi Kumari, Guttena Veerabhadram, Kotu Girija Mangatayar, A novel green synthesis of silver nanoparticles using Gum Karaya: characterization, antimicrobial and catalytic activity studies, J. Clust. Sci. (2013), https://doi.org/10.1007/s10876-013-0620-1.

[6] M.H.N. Assadi, H. Katayuma-Yoswda, Sodium cobaltite engineered with alkaline earth metal doping for waste energy harvesting; a theoretical study, Energy Procedia (2015) 75.

[7] R. Mani, High photocatalytic activity of pure and Ni doped SnO2 nanoparticles by a facile wet chemical -route, J. Mat. Sci. -Mater. Electron. (2018).

[8] Jincheng Yu, Robert Freer, Calcium cobaltite, a promising oxide for energy harvesting: effective strategies toward enhanced thermoelectric performance, J. Phys. Energy 4 (2022) 022001, https://doi.org/10.1088/2515-7655/ac5172.

[9] Xiaokun Huang and Weiyi Zhang, How does the spin-state of Co ions affect the insulator-metal transition in Bi2A2Co2O8 (A = Ca, Sr, Ba), Scientific Rep. | 6: 38212 | DOI:10.1038/srep3821.

[10] O. Polat, M. Coskun, F.M. Coskun, J. Zlamal, Z. Durmus, M. Caglar, A. Turut, Influence of transition element Os substitution on the structural and electrical features of perovskite structure $LaCr_{1-x}Os_xO_3$, Mat. Res. Bull. 124 (2020), https://doi.org/10.1016/j.materresbull.2019.110759.

[11] H.A. Alluhaybi, S.K. Ghoshal, B.O. Alsobhi, W.N. Wan Shamsuri, Visible photoluminescence from gold nanoparticles: a basic insight, Opt. - Int. J. Light Electron Opt. 192 (2019) 162936, https://doi.org/10.1016/j.ijleo.2019.162936.

[12] Antariksh Saxena, R.M. Tripathi, R.P. Singh, A biological synthesis of silver nanoparticles by using onion (Allium cepa) extract and their antibacterial activity, Dig. J. Nanomater. Biostruct. 5 (2) (2010) 427–432.

[13] Yiing Yee Foo, Vengadesh Periasamy, Lik Voon Kiew, G.Gnana Kumar, Sri Nurestri, Abd Malek, Curcuma mangga-mediated synthesis of gold nanoparticles: characterization, stability, cytotoxicity, and blood compatibility, Nanomaterials 7 (6) (2017) 123, https://doi.org/10.3390/nano7060123.

[14] Paulo Carvillo, Yun Chen, Cullen Boyle, Paul N. Barnes, Xueyan Song, Thermoelectric performance enhancement of calcium cobaltite through barium grain boundary segregation, Inorg. Chem. 54 (2015) 9027, https://doi.org/10.1021/acs.inorgchem.5b01296.

[15] Takuya Fujima, Hideki Arimatsu, Shota Miura, Shun Yokoyama, Ken-ichi Takagi, n-p type variation in thermoelectric $AlMgB_{14}$ based materials by raw material mixture ratio, Solid State Sci. 47 (2015) 51.

[16] NingYu Wu, Tim C. Holgate, Ngo Van Nong, Nini Pryds, S.øren Linderoth, High-temperature thermoelectric properties of $Ca_3Co_4O_{9+\delta}$ by auto-combustion synthesis and spark plasma sintering, J. Eur. Ceram. Soc. 34 (2014) 925, https://doi.org/10.1016/j.jeurceramsoc.2013.10.022.

[17] Rafiq Fareenpoornima, G. Parthipan, S. Periyasamy, Synthesis of a novel nanoparticle $BaCoO_{2.6}$ through the sol-gel method and elucidation of its structure and electrical properties, J. Nano Mater. (2022), https://doi.org/10.1155/2022/3877879.

[18] Rafiq Fareenpoornima, S. Deborah, G. Parthipan, First principal study of conduction mechanism of Mg-doped BaCoO2.6 nanoparticles, J. Mater. (2024).

[19] Kouta Iwasaki, Teruhisa Yamamoto, Hisanori Yamane, Takashi Takeda, Shigeo Arai, Hidetoshi Miyazaki, Kazuyoshi Tatsumi, Masahito Yoshino, Tsuyoshi Ito, Yuji Arita, Shunsuke Muto, Takanori Nagasaki, Tsuneo Matsui, Thermoelectric properties of $Ba_3Co_2O_6(CO_3)_{0.7}$ containing one-dimensional CoO_6 octahedral columns, J. Appl. Phys. 106 (2009) 034905, https://doi.org/10.1063/1.3174428.

[20] R.A.M. Machado, M.V. Gelfuso, D. Thomazini, Thermoelectric properties of barium doped calcium cobaltite obtained by simplified chemical route, Cerâmica 67 (2021) 90–97, https://doi.org/10.1590/0366-69132021673813034.

[21] K. Boulahya, M. Parras, J.M. Gonzalez-Calbet, New commensurate phases in the family ($A_3Co_2O_6$) or ($A_3Co_3O_9$) (A = Ca.Sr,Ba), Chem. Mater. 12 (2000) 25–32, https://doi.org/10.1021/cm991028g.

[22] Vineet Singh, Pratima Chauhan, Structural and optical characterization of CdS nanoparticles prepared by chemical precipitation method, J. Phys. Chem. Solids 70 (2009) 1074–1079, https://doi.org/10.1016/j.jpcs.2009.05.024.

[23] A.S. Garde, Large-scale synthesis and characterization of cadmium sulfide nanoparticles by simple chemical route, Nanosyst.: Phys., Chem., Math. 11 (4) (2020) 444–452.

[24] Fu Li, Jing-Feng Li, Effect of Ni substitution on electrical and thermoelectric properties of $LaCoO_3$ ceramics, Ceram. Int. 37 (2011) 105, https://doi.org/10.1016/j.ceramint.2010.08.024.

[25] F. Khatun, M.A. Gafur, M.S. Alia, M.S. Islam, M.A.R. Sarker, Impact of Lithium composition on structural, electronic and optical properties of lithium cobaltite prepared by solid-state reaction, J. Sci. Res. 6 (2014) 217, https://doi.org/10.3329/jsr.v6i2.17900.

[26] Jincheng Yu, Kan Chen, Feridoon Azough, Diana T. Alvarez-Ruiz, Michael J. Reece, Robert Freer, Enhancing the thermoelectric performance of calcium cobaltite ceramics by tuning composition and processing, ACS Appl. Mater. Interfaces 12 (42) (2020) 47634, https://doi.org/10.1021/acsami.0c14916.

[27] Sumaiyah Megat Nabil Mohsin, Mohd Zobir Hussein, Siti Halimah Sarijo, Sharida Fakurazi, Palanisamy Arulselvan, Yun Hin Taufiq-Yap, Nanolayered composite with enhanced ultraviolet ray absorption properties from simultaneous intercalation of sunscreen molecules, Int. J. Nanomed. 13 (2018) 6359, https://doi.org/10.2147/IJN.S171390.

[28] C.H. Yeo, S.H.S. Zein, A.L. Ahmed, Investigation into the role of NaOH and calcium ions in the synthesis of calcium phosphate nanoshells, Braz. J. Chem. Eng. 29 (2012) 147.

[29] Abhishek Mathur, Akhilesh Kushwaha, Vandana Dalakoti, Garima Dalakoti and Deep Shikha Singh, Green synthesis of silver nanoparticles using medicinal plant and its characterization, Pelagia Res. Libr. Der Pharm. Sin. 5 (5) (2014) 118–122. ISSN: 0976-8688.

[30] G. Motas, Nima E. Gorji, Dumitru Nedelcu, Dermot Brabazon, Fabrizio Quadrini, XPS, SEM, DSC and nanoindentation characterization of silver nanoparticle-coated biopolymer pellets, Appl. Sci. 11 (16) (2021) 7706, https://doi.org/10.3390/app11167706.

[31] Ålma Laura González-Mendoza, Lourdes I. Cabrera-Lara, Reaction parameters for controlled sonosynthesis of gold nanoparticles, J. Mex. Chem. Soc. 59 (2) (2015) 119–129, https://doi.org/10.29356/jmcs.v59i2.25.

[32] Ericka Rodríguez-León, Ramón Iñiguez-Palomares, Rosa Elena Navarro, Ronaldo Herrera-Urbina, Judith Tánori, Claudia Iñiguez-Palomares, Amir Maldonado, Synthesis of silver nanoparticles using reducing agents obtained from natural sources (Rumex hymenosepalus extracts), Nanoscale Res Lett. 8 (2013) 318, https://doi.org/10.1186/1556-276X-8-318.

[33] Fatemeh Sadat Razavi, Azam Sobhani, Omid Amiri, Maryam Ghiyasiyan-Arani, Masoud Salavati-Niasari, Green sol-gel auto-combustion synthesis, characterization and investigation of the electrochemical hydrogen storage properties of barium cobalt oxide nanocomposites with maltose, Int. J. Hydrog. Energy (2020), https://doi.org/10.1016/j.ijhydene.2020.04.273.

[34] P.B. Rathod, S.A. Waghuley, Synthesis and UV-Vis spectroscopic study of TiO_2 nanoparticles, Int. J. Nanomanuf. 11 (3/4) (2015).

[35] N.S. Wadatkar, S.A. Waghuley, Complex optical studies on conducting polyindole as-synthesized through chemical route, EJBAS (2015) 1–6, https://doi.org/10.1016/j.ejbas.2014.12.006.

[36] Shalini Agarwal, Y.K. Saraswat, Vibhav K. Saraswat, Study of optical constants of ZnO dispersed PC/PMMA blend nanocomposites, Open Phys. J. 3 (2016) 63–72.

[37] Mayumi M. Nakata, Tatiana M. Mazzo, Graziela P. Casali, Felipe A. La Porta, Elson Longo, A large red-shift in the photoluminescence emission of $Mg_{1-x}Sr_xTiO_3$, Chem. Phys. Lett. 622 (2015) 9–14, https://doi.org/10.1016/j.cplett.2015.01.011.

[38] N. Ramjeyanthi, M. Alagar, D. Muthuraman, Synthesis, structural and optical behavior of cerium oxide nanoparticles by co-precipitation method, Int. J. Sci. Res. Sci. Technol. 4 (5) (2018) 44–51.

[39] Seema Verma, K.K. Bamzai, Preparation of Cerium orthophosphate nanosphere by co-precipitation route and its structural, thermal, optical, and electrical characterization, J. Nanopart. (2014), https://doi.org/10.1155/2014/125360.

[40] Neama Gomaa Imam, Salwa Mohamed Ismail, Mohammed Yehia Elbahrawy, Adel Mohammed Hashhash, Photoluminescence, magnetic and electrical properties of Co-ferrite nanoparticles synthesized via sol-gel auto-combustion method, Int. J. Nanopart. 7 (¾) (2014).

[41] Iffat Ameen, Abhishek Kumar Tripathi, Raj Laxmi Mishra, Afshan Siddiqui, Umesh Nath Tripathi, Luminescent, optical, magnetic and metamaterial behavior of cerium complexes, J. Saudi Chem. Soc. 23 (2019) 725–739, https://doi.org/10.1016/j.jscs.2018.12.003.